Giant plasmonic bubbles nucleation under different ambient pressures

Binglin Zeng [1,2,3,4] Yuliang Wang [1,2,3,*] Mikhail E. Zaytsev,[2,4] Chenliang Xia [1]
Harold J. W. Zandvliet [4,†] and Detlef Lohse [2,5,‡]

[1]*School of Mechanical Engineering and Automation, Beihang University, 37 Xueyuan Rd, Haidian District, Beijing, China*
[2]*Physics of Fluids Group, Department of Applied Physics and J. M. Burgers Centre for Fluid Dynamics,*
University of Twente, P.O. Box 217, 7500 AE Enschede, The Netherlands
[3]*Beijing Advanced Innovation Center for Biomedical Engineering, Beihang University, 37 Xueyuan Rd, Haidian District, Beijing, China*
[4]*Physics of Interfaces and Nanomaterials, MESA+ Institute for Nanotechnology, University of Twente, 7500 AE Enschede, The Netherlands*
[5]*Max Planck Institute for Dynamics and Self-Organization, Am Fassberg 17, 37077 Göttingen, Germany*

Water-immersed gold nanoparticles irradiated by a laser can trigger the nucleation of plasmonic bubbles after a delay time of a few microseconds [Wang *et al.*, Proc. Natl. Acad. Sci. USA **122**, 9253 (2018)]. Here we systematically investigated the light-vapor conversion efficiency, η, of these plasmonic bubbles as a function of the ambient pressure. The efficiency of the formation of these initial-phase and mainly water-vapor containing bubbles, which is defined as the ratio of the energy that is required to form the vapor bubbles and the total energy dumped in the gold nanoparticles before nucleation of the bubble by the laser, can be as high as 25%. The amount of vaporized water first scales linearly with the total laser energy dumped in the gold nanoparticles before nucleation, but for larger energies the amount of vaporized water levels off. The efficiency η decreases with increasing ambient pressure. The experimental observations can be quantitatively understood within a theoretical framework based on the thermal diffusion equation and the thermal dynamics of the phase transition.

I. INTRODUCTION

Water-immersed noble-metal nanoparticles under irradiation of continuous-wave lasers can rapidly produce large amounts of heat when the plasmon resonance frequency of the nanoparticle matches with the laser frequency, resulting in the explosive boiling of water surrounding the nanoparticles. This explosive boiling results in the nucleation and growth of so-called plasmonic bubbles [1–6]. These plasmonic bubbles are of great importance in numerous plasmonic-enhanced applications, ranging from cancer therapeutics [7–10], catalytic reactions [11], micromanipulation of nano-objects [12–14], and solvothermal chemistry [1]. They also have been proposed for the conversion of solar energy [15–21]. In all these applications, light-induced vapor formation plays a key role. How efficiently the light can be converted into vapor during this process remains, however, unclear. The light-vapor conversion efficiency is related to the growth dynamics of the plasmonic bubbles as well as the physicochemical properties of the surrounding liquid [22].

Previous studies on plasmonic bubble formation and growth dynamics have mainly focused on the milliseconds to seconds timescale [2,4,5,17]. Plasmonic bubbles formed on these timescales are hereafter referred to as ordinary plasmonic bubbles. In one of our previous studies we have shown that the growth of these ordinary plasmonic bubbles in water can be divided into two phases, a vaporization-dominated phase and a gas-diffusion dominated phase [23]. Plasmonic bubbles in the former phase have a smaller size. Water in the vicinity of the three-phase contact line is in direct contact with the laser spot. A relatively large fraction of the energy dumped in the nanoparticles is used to vaporize the surrounding water. As a result, these bubbles mainly contain vapor and exhibit a relatively high light-vapor conversion efficiency. In contrast, later the ordinary plasmonic bubbles contain both vapor and gas and are substantially larger. Therefore, the laser spots are then completely isolated from the water by the growing plasmonic bubbles [24]. Consequently, the heat at the laser spots cannot be directly transferred into the surrounding liquid. This significantly reduces the light-vapor conversion efficiency. As a result, the diffusion of dissolved gas expelled from the surrounding liquid dominates the growth of the plasmonic bubbles; consequently, they mainly contain gas and the light-vapor conversion efficiency of this phase is substantially lower than in the vapor-dominated phase.

We recently analyzed the very initial plasmonic bubble phase on a time scale of microseconds [6]. In this very initial phase a giant plasmonic bubble forms after a short delay time after switching on the laser, with a growth rate that is about three orders of magnitude larger than the ordinary plasmonic bubbles [6]. The lifetime of these initial phase plasmonic bubbles is, however, very short. Shortly after their formation they collapse due to the condensation of vapor [6].

The relatively large light-vapor conversion efficiency and the explosive growth rate of the giant initial plasmonic

*wangyuliang@buaa.edu.cn
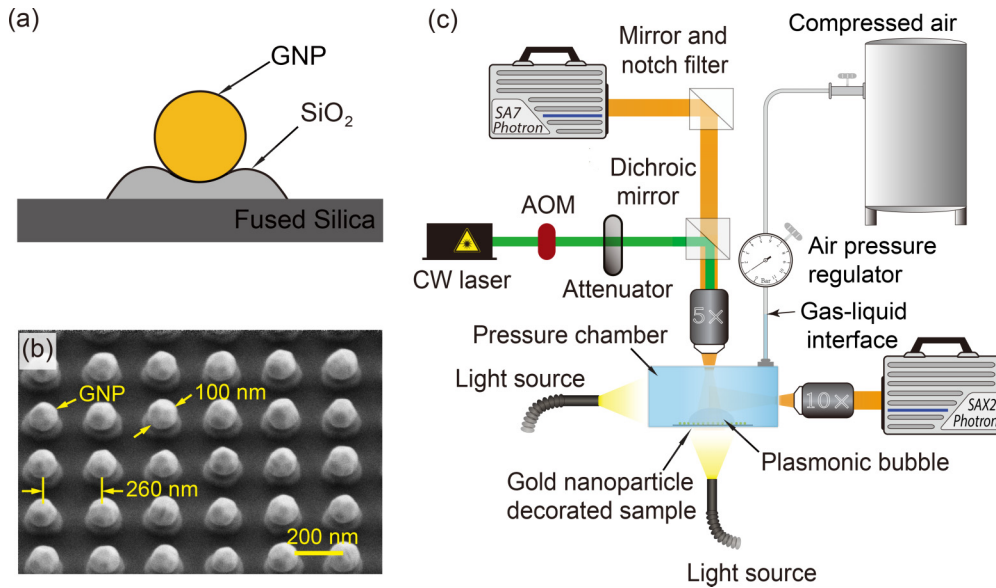†h.j.w.zandvliet@utwente.nl
‡d.lohse@utwente.nl

FIG. 1. (a) Schematic of a gold nanoparticle sitting on a SiO$_2$ island. (b) A scanning electron microscopy image of the gold nanoparticle decorated substrate. (c) Schematic of the optical-imaging facilities for giant initial bubble observation under different ambient pressures. A pressure chamber is used to tune the pressure from 1 to 9 bar. A narrow tube together with an elevated gas-liquid interface significantly slows down gas diffusion from the compressed air to the water in the pressure chamber. As a result, the gas concentration of the water in the pressure chamber remains almost constant throughout the experiments.

bubbles makes them very interesting for numerous applications. However, the underlying mechanism for their formation, as well as the light-vapor conversion process during bubble nucleation, are not quantitatively understood yet. Among the various physicochemical properties of the liquid such as the latent heat, obviously also the boiling point is very relevant for the nucleation and formation of plasmonic bubbles. However, it is very challenging to tune the boiling point of a liquid without changing the other physicochemical properties. Here we have varied the boiling point of water from 100 to 175°C by changing the ambient pressure from 1 to 9 bar. We have studied the nucleation and growth of the initial giant plasmonic bubbles under different ambient pressures and laser powers in order to obtain a thorough and solid understanding of the bubble nucleation as well as the light-vapor conversion processes.

II. EXPERIMENTAL SYSTEM

A. Sample preparation

A gold layer of ∼45 nm was deposited on an amorphous fused-silica wafer by using an ion-beam sputtering system (home-built T′COathy machine, MESA$^+$, Twente University). The wafer was coated with a bottom antireflection coating (BARC) layer (∼186 nm) and a photoresist (PR) layer (∼200 nm). Periodic nanocolumns with diameters of ∼110 nm were patterned in the PR layer by using displacement Talbot lithography (PhableR 100C, EULITHA) [25]. Subsequently, these periodic PR nanocolumns were transferred to the underlying BARC layer, forming 110-nm BARC nanocolumns by using nitrogen plasma etching (home-built TEtske machine, NanoLab) at 10 mTorr and 25 W for 8 min. Taking these BARC nanocolumns as a mask, the Au layer was then etched by ion-beam etching (Oxford i300, Oxford

Instruments, United Kingdom) with 5-sccm Ar and 50–55 mA at an inclined angle of 5°. The etching for 9 min resulted in periodic Au nanodots supported on cone-shaped fused-silica features. The remaining BARC was stripped using oxygen plasma for 10 min (TePla 300E, PVA TePla AG, Germany). The fabricated array of Au nanodots was annealed to 1100°C in 90 min. and subsequently cooled passively to room temperature. During the annealing process, these Au nanodots reformed into spherical-shaped Au nanoparticles, as shown in Figs. 1(a) and 1(b).

B. Setup description

Figure 1(c) shows a schematic diagram of the experimental setup used for the study of initial giant bubbles under different ambient pressures p_0. In the setup, the gold nanoparticle decorated substrate was placed in a home-built pressure chamber. The chamber was completely filled with deionized (DI) water (Milli-Q Advantage A10 System, Germany) and connected to the compressed air via a narrow tube. Before the experiments, the DI water was exposed to air for 24 h to obtain fully air-saturated water. The gas concentration in the DI water was measured by an oxygen meter (Fibox 3 Trace, PreSens). The measured relative air concentration level was 0.99. The pressure of the chamber was tuned by an air-pressure regulator. Here we have used seven different ambient pressures of 1, 2, 3, 4, 5, 7, and 9 bar, respectively. A continuous-wave laser (Cobolt Samba) with a wavelength of 532 nm was used for irradiation of our samples. The radius R_l of the laser spot was about 12.5 μm. The laser power P_l projected on the sample surface was tuned via two polarization filters and measured by a photodiode power sensor (S130C, ThorLabs). Laser pulses of 10 ms were generated by a pulse–delay generator (BNC model 565).

Two high-speed cameras were used for top view and side-view imaging, respectively. The top-view camera (SA7, Photron) was used to focus the laser on the sample surface, while the side-view camera (SAX2, Photron) was used for the observation of the formation of bubbles. The top-view camera and the side-view camera were equipped with a 5× (LMPLFLN, Olympus) and a 10× (SLMPLN, Olympus) long working distance objectives, respectively. A frame rate of 540 kfps was used for side-view imaging. A home-designed algorithm was applied to segment the acquired bubble images [26–28]. With this algorithm, the bubble volume can be extracted automatically.

III. RESULTS AND DISCUSSION

Several images of initial giant bubbles at their maximum size at the same laser power P_l of 32.7 mW, but under different ambient pressures, p_0, are shown in Fig. 2(a). These results show that the maximum size of the giant bubble rapidly decreases with increasing p_0, reflecting that with increasing ambient pressure p_0 the expanding has to do more work against the ambient pressure. As we have previously reported, the volume of the initial phase giant bubbles is directly related to the delay time, τ_d, which is defined as the time interval between switching on the laser and the nucleation of the bubble [6]. In Fig. 2(b) a semilogarithmic plot of τ_d as a function of laser power P_l is shown. As already seen in Ref. [6], the delay time, τ_d, decreases with increasing laser power P_l, but here we find that τ_d is independent of p_0 for a fixed P_l in the range of 1 to 9 bar; see Fig. 2(c). We noticed that the measured delay time for all three laser powers under 5 bar is relatively higher than for the other pressure values. We speculate that this is a systematic error, presumably originating from the laser spot under 5 bar being slightly out of focus, leading to a slightly lower laser power density and hence increased delay time.

Before bubble nucleation, the water has to be heated up to the nucleation temperature T_n, which usually substantially exceeds the boiling temperature T_{boil} [29–31]. The higher the laser power P_l, the faster the surrounding water heats up and the shorter the delay time τ_d. The nucleation temperature T_n can be numerically determined; for details, see Refs. [6,22]. The spatial-temporal evolution of the temperature of water, $T(r, t)$, surrounding a gold nanoparticle that is heated by a laser can be numerically calculated by solving the heat-diffusion equation,

$$\partial_t(T(r,t)) = \frac{P_l(r,t)}{\rho c_p} + \kappa \frac{1}{r^2}\partial_r(r^2\partial_r T(r,t)), \quad (1)$$

where κ, ρ, and c_p are thermal diffusivity, density, and heat capacity of water, r is the distance to the nanoparticle, t is the time, and $P_l(r, t)$ the laser power density (in W/m^3). For the numerical solution of the partial differential equation (1), as spatial boundary condition we took the specific configuration of the gold nanoparticle decorated sample surface used in the experiment. The heat conductivity of water and fused silica are 0.61 and 1.38 W/(mK), respectively. This simple thermal diffusion model does not include the interfacial thermal resistance term (Kapitza), which does not play a role here because our timescale exceeds the timescale of the study reported in Ref. [32] (where it is considered) by several orders of mag-
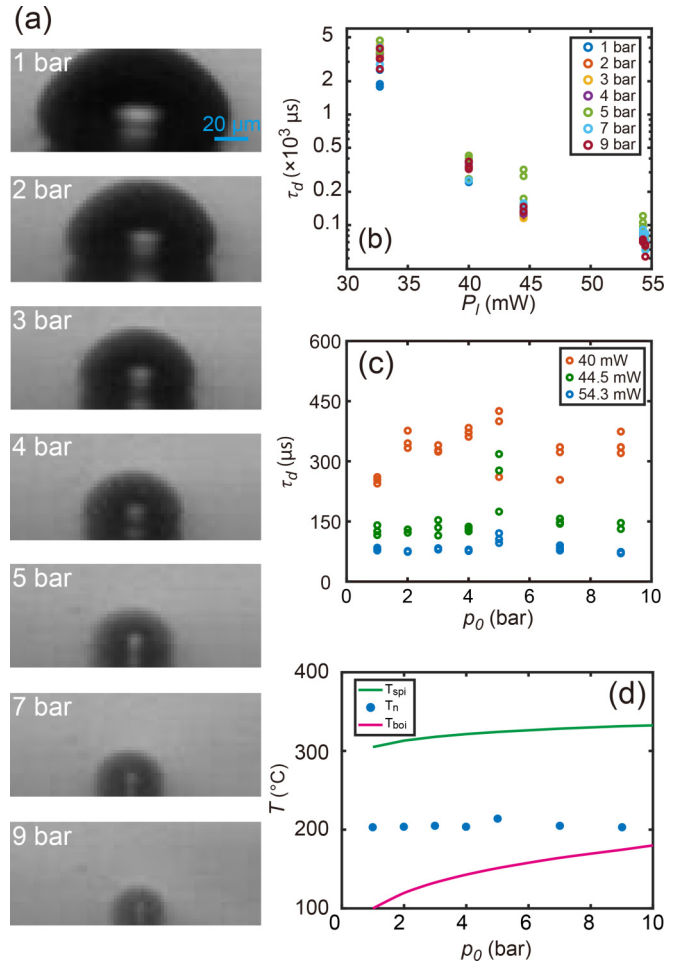

FIG. 2. (a) Examples of side-view images of initial giant bubbles at the same laser power $P_l = 32.7$ mW, but at different ambient pressures p_0 (see legend). The respective snapshots were taken at the maximum of the bubble expansion. (b) Delay time τ_d vs P_l at different ambient pressures. (c) Delay time τ_d vs p_0 at different values of P_l (see legend). (d) Bubble nucleation temperature T_n vs the ambient pressure p_0. The nucleation temperature T_n is obtained by fitting τ_d with the numerical model. It is found to be independent of p_0. We also show the spinodal temperature T_{spi}, i.e., the theoretical maximal attainable temperature of the liquid without vapor bubble nucleation.

nitude. The temperature field $T(r, t)$ generated by an array of nanoparticles can be considered as the linear superposition of the temperature distribution fields of the individual gold nanoparticles within a Gaussian laser beam profile,

$$T(x, y, z, t) = \sum_{i=1}^{N_{np}} [T_i(d_{i,(x,y,z)}, t)], \quad (2)$$

where N_{np} is the number of gold nanoparticles under laser irradiation, T_i is the temperature field produced by the *i*th nanoparticle, and d_i is the distance to the center of the *i*th nanoparticle. Note that the delay time before the initial plasmonic bubble nucleation is more than 50 μs, which is much longer than the thermal relaxation time of 10 $\sim$ 100 ps for the electrons in the metal nanoparticles mentioned in Ref. [33].
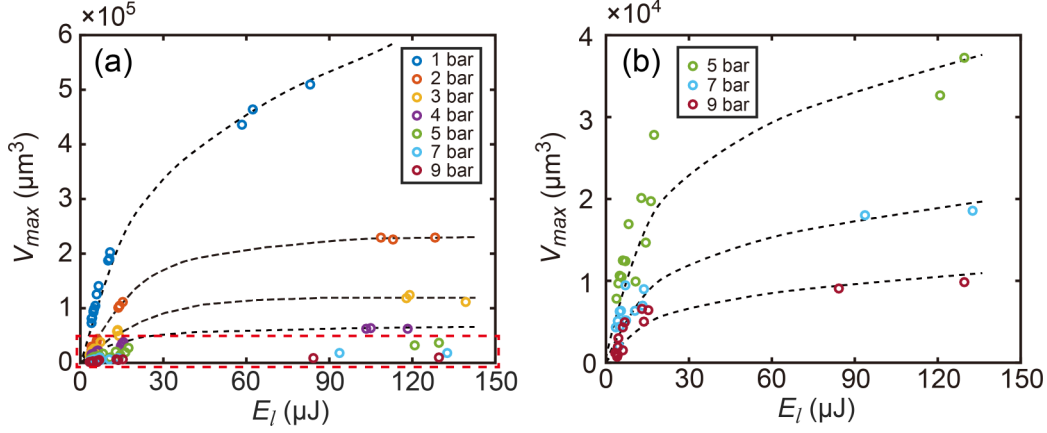
FIG. 3. (a) Maximum volume V_{max} of the bubbles as a function of the total deposited laser energy E_l under different ambient pressures p_0 (see legend) ranging from 1 to 9 bar. (b) Zoomed-in version of the same plot curves for $p_0 = 5$, 7, and 9 bar [red dashed box in (a)]. All curves exhibit two regimes, namely a linear regime and a nonlinear regime, irrespective of the value of p_0. The dashed lines are drawn to guide the eye.

Therefore, the thermal relaxation effect of the GNPs close to the border of the laser beam can be neglected in this system.

As shown in Ref. [6], by numerically solving Eqs. (1) and (2), one can directly obtain the time required to reach the nucleation temperature of water at a given laser power. This approach was employed for all the experimental data using a root-mean-square minimization method. In this way, T_n was obtained for different ambient pressures and is shown in Fig. 2(d). Interestingly, T_n is independent of the ambient pressure and has values around 200°C.

In addition, the results shown in Figs. 2(b)–2(d) also provide insight into the dependence of T_n on the amount of dissolved gas in water. Previous studies have shown that τ_d strongly depends on the gas concentration in water [6,34]. In the experiments, the absolute gas concentration is independent of the ambient pressure, p_0, as we do not give the water the time to be equilibrated after changing the ambient pressure. We, therefore, arrive at the conclusion that the nucleation temperature mainly depends on the absolute amount of dissolved gas in the water, which here does not depend on p_0.

The maximum volume V_{max} of the bubbles as a function of the total deposited energy $E_l = P_l \tau_d$ for different values of p_0 is shown in Fig. 3(a). Figure 3(b) shows three curves [enclosed by the red dashed box in Fig. 3(a)] for ambient pressures of 5, 7, and 9 bar, respectively. One can see that, regardless of the exact value of p_0, all curves exhibit a qualitatively $V_{\mathrm{max}}(E_l)$ dependence. When E_l is smaller than $20\,\mu$J, V_{max} linearly increases with E_l, which is consistent with our previous study [6,34]. However, when E_l is larger than $20\,\mu$J, $V_{\mathrm{max}}(E_l)$ dependence becomes nonlinear.

In the linear regime, the amount of water vapor in the bubbles is proportional to E_l. The proportionality factor k between energy and maximum bubble volume can be used to estimate the light-vapor conversion efficiency η. The linear regime of the $V_{\mathrm{max}}(E_l)$ curves for different values of p_0 are shown in Fig. 4(a). The extracted proportionality factor k as a function of p_0 is shown in Fig. 4(b). It can be seen that k rapidly decreases from $1.9 \times 10^4\,\mu$m$^3/\mu$J to $440\,\mu$m$^3/\mu$J when p_0 is increased from 1 to 9 bar.

We now define the efficiency η as the ratio of the energy E_b used for water vaporization during vapor bubble formation to the energy E_d deposited in the gold nanoparticles before nucleation of the bubble, i.e., $\eta = E_b/E_d$. Considering a gold nanoparticle coverage of $\xi = 11.6\%$, we have $E_d = \xi E_l$, where E_l is the total deposited laser energy on the sample surface. The value η can then be written as

$$\eta = \frac{E_b}{\xi E_l}. \tag{3}$$

The energy E_b required to vaporize the water is composed of two components. One component is the energy needed to heat the water to vaporization temperature and the other component deals with the phase transition of the water from liquid to vapor, i.e., the latent heat H_{vap}. Consequently, E_b for a vapor bubble is given by

$$E_b = \left(\int_{T_0}^{T_{\mathrm{sat}}} c_p dT + H_{\mathrm{vap}} \right) \frac{M p_{\mathrm{sat}} V_{\mathrm{max}}}{R_g T_{\mathrm{sat}}}, \tag{4}$$

where T_0 and T_{sat} are the ambient temperature and saturation temperature of water, respectively. M is the molar mass of water (18 g/mol) and p_{sat} is the saturation pressure of water vapor at the moment that the bubble reaches its maximum volume. V_{max} is the maximum volume of the bubble and $R_g = 8.314\,$J/(mol K) the universal gas constant. By combining Eqs. (3) and (4), we find

$$\eta = \left(\int_{T_0}^{T_{\mathrm{sat}}} c_p dT + H_{\mathrm{vap}} \right) \frac{M p_{\mathrm{sat}} V_{\mathrm{max}}}{R_g T_{\mathrm{sat}} \xi E_l}. \tag{5}$$

To calculate η from Eq. (5), we note that the saturation pressure p_{sat} is close to the ambient pressure p_0 and can be estimated to be $p_0 - 0.04$ bar [6]. Once p_{sat} is determined, T_{sat} can be obtained [Fig. 4(c)] [35]. The ratio $p_{\mathrm{sat}}/T_{\mathrm{sat}}$ is dependent on p_0. The efficiency can be obtained using the prefactor k for the linear regime in the $V_{\mathrm{max}}(E_l)$ dependence at a given p_0. The obtained efficiency as a function of p_0 is shown in Fig. 4(d). The efficiency decreases from 25 to 5% when p_0 is increased from 1 to 9 bar.
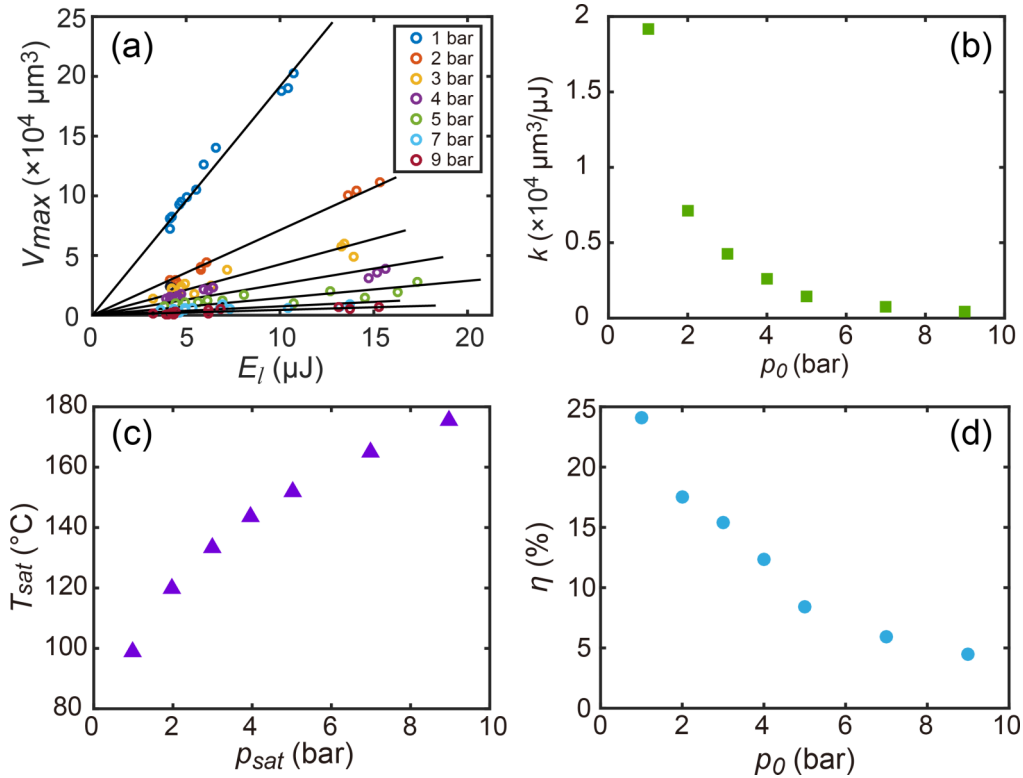
FIG. 4. (a) The maximum volume $V_{\max}$ of the giant bubbles as a function of E_l in the linear regime under different ambient pressures p_0 (see legend). (b) The prefactor $k = V_{\max}/E_l$ of the linear relation $V_{\max}$ vs E_l as a function of p_0. (c) Saturation temperature T_{sat} vs saturation pressure, p_{sat}, at the moment of maximum giant bubble volume under different ambient pressure p_0. (d) Experimentally obtained light-vapor conversion efficiencies η vs the ambient pressure p_0.

In the nonlinear regime of the $V_{\max}(E_l)$ dependences, k is still defined as $V_{\max}/E_l$ and obviously depends on E_l and also p_0. Following Eq. (5), the light-vapor conversion efficiency changes accordingly. For the experimental results shown in Fig. 3, the corresponding efficiency as a function of laser power P_l and ambient pressure p_0 is presented in Fig. 5, revealing that the efficiency decreases with increasing p_0 and decreasing P_l.

To better understand how P_l and p_0 affect η during the nucleation of the initial phase giant bubbles, we numerically solve Eqs. (1) and (2) for a whole range of P_l and p_0. An exam-
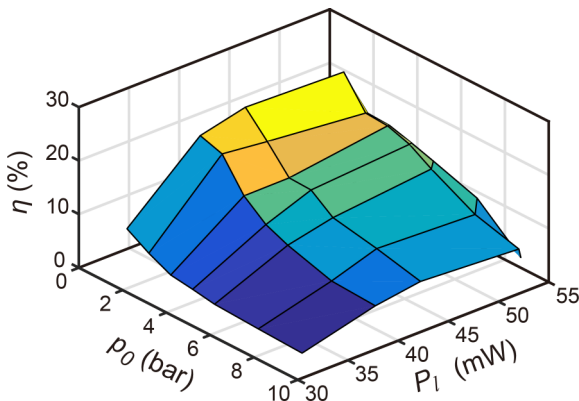

FIG. 5. The experimentally measured light-vapor conversion efficiency, η, as a function of laser power P_l and ambient pressure p_0.

ple of the constructed temperature distribution field is shown in Fig. 6(a). From this figure, one can see that the temperature of the water rapidly decreases with increasing distance away from the center of the laser spot. In our model, we assume that the following two conditions are valid during the nucleation of the bubble: (1) the bubble starts to nucleate when the highest temperature of the surrounding water has reached the nucleation temperature T_n, (2) the volume of the bubble is determined by the amount of water that has a temperature higher than an ambient pressure-dependent threshold temperature, which is defined as vaporization temperature T_{vap}. In Fig. 6(b), a zoom-in plot of the temperature distribution of the red dashed box in Fig. 6(a) is shown. The key question is of course how to determine T_{vap}.

Given a certain water temperature distribution, the value T_{vap} determines the amount of water that can be vaporized in case a bubble nucleates. A higher value of T_{vap} implies a smaller volume of water and thus a smaller bubble. Therefore, the maximum size of the bubble allows us to determine T_{vap}. The amount of moles of vaporized water molecules $n_{\max,\exp}$ in a giant bubble is given by

$$n_{\max,\exp} = \frac{p_{\text{sat}} V_{\max}}{R_g T_{\text{sat}}}. \tag{6}$$

$n_{\max,\exp}$ as a function of E_l for different pressures p_0 is plotted in Fig. 6(c) (circles refer to the experimental data). It clearly shows that for a given laser energy E_l the amount of vaporized water decreases with increasing p_0. For higher values of the
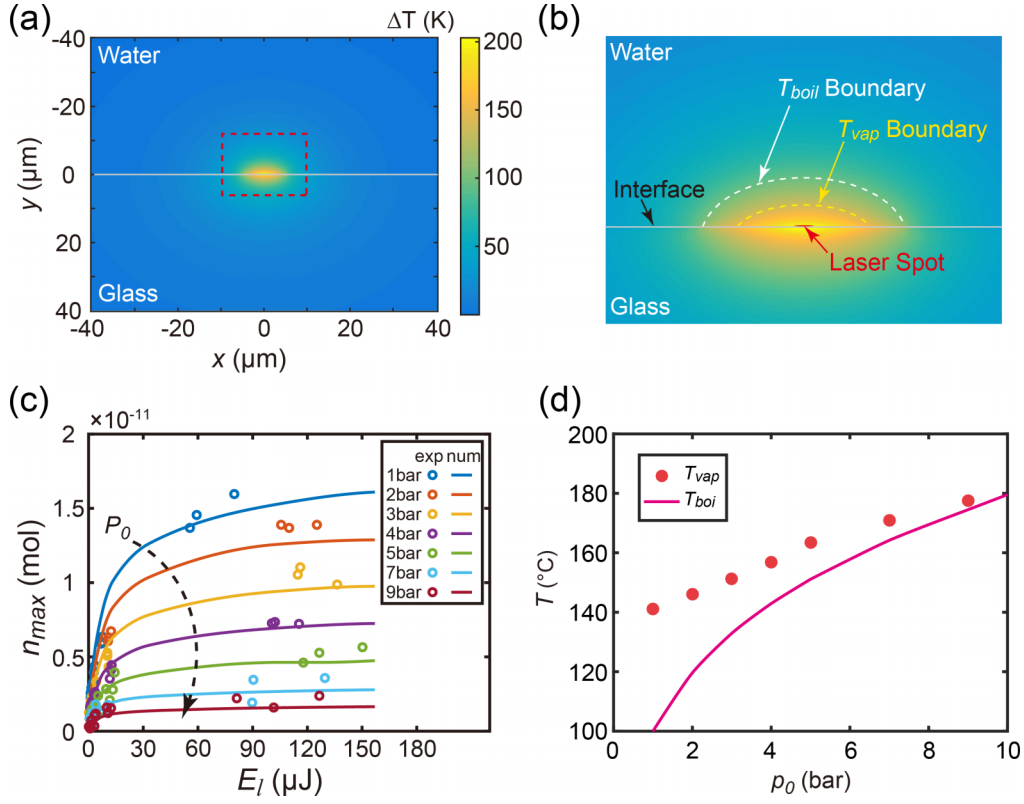
FIG. 6. (a) Water temperature field in the vicinity of a laser spot constructed by numerically solving the model discussed in the text. (b) Enlarged view of the water temperature field [dashed red box in panel (a)]. Once the water temperature at the impact point of the laser reaches T_n, water within the regime with boundary of T_{vap} rapidly vaporizes and a giant bubble is nucleated. (c) Experimentally measured (data points) and numerically calculated (curve) amount of vaporized water in moles, n_{max}, as a function of the total deposited laser energy E_l for various ambient pressures p_0 (see legend). (d) Vaporization temperature T_{vap} and boiling point T_{boil} vs ambient pressure p_0.

laser energy E_l, $n_{max,exp}$ levels off. The above two observations are consistent with the obtained $\eta(P_l)$ and $\eta(p_0)$ dependences.

The thermal diffusivity κ and specific heat capacity c_p of water only very weakly depend on the ambient pressure (Table I in the Appendix). We have shown that the nucleation temperature T_n is independent of the ambient pressure. Based on these dependences the water temperature distribution is independent of the ambient pressure p_0 for a fixed laser power P_l. The temperature distribution in the water depends, however, on the laser power. Upon selecting a value for T_{vap} the amount of water molecules can be calculated, which implies that we can extract $n(T_{vap})$ for each laser power. The total deposited laser energy in the numerical calculation is given by $E_l = P_l \tau_d$. Subsequently, the $n(E_l)$ dependence can be obtained by gradually tuning T_{vap} from room temperature to T_n for each value of P_l. Using the $n(E_l)$ dependence, $T_{vap}(p_0)$ can be determined by minimizing $\Sigma[n(E_l) - n_{max,exp}(E_l)]^2$. The results are displayed in Fig. 6(c). The numerically determined $n_{max}(E_l)$ dependence agrees well with the experimentally obtained results.

The numerically determined T_{vap} for different ambient pressures is shown in Fig. 6(d). The solid circles refer to the numerically determined T_{vap}, while the solid curve represents the water boiling point T_{boil} as a function of p_0. It is clear that T_{vap} is in between T_{boil} and T_n [around 200°C, as shown in Fig. 2(d)]. With increasing p_0, the vaporization temperature T_{vap} gets closer to T_n.

We now return to the observed dependences of η on the laser power P_l and the ambient pressure p_0. A higher laser power P_l leads to a faster increase of the water temperature and to a short delay time τ_d. If τ_d is small compared to the thermal diffusion timescale $\tau_{diff} \approx R_l^2/(\pi\kappa)$, only a small amount of energy can diffuse into the nonvaporizable zone, resulting in a high efficiency. On the contrary, a lower laser power P_l leads to a longer delay time τ_d. Since the thermal diffusivity κ is almost independent of the ambient pressure, an increased delay time τ_d results in an increased amount of energy diffusion into the nonvaporization zone and hence a lower efficiency. Regarding the ambient pressures p_0, a higher value will lead to an increased vaporization temperature T_{vap}. As a result, a reduced portion of heated water will be vaporized. Although the delay time of bubble nucleation remains constant for different ambient pressures, the portion of laser energy used for water vaporization decreases, resulting in a decreased light-vapor conversion efficiency.

IV. CONCLUSIONS

We have systematically investigated the nucleation of initial giant plasmonic bubbles in water with boiling points ranging from 100 to 175°C by tuning ambient pressure from 1 to 9 bar. The experimental observations can be quantitatively understood within a theoretical framework based on the thermal diffusion equation and the thermodynamics of

the phase transition. It has shown that water in the vicinity of laser-irradiated gold nanoparticles can be divided into a vaporization zone and a nonvaporization zone. The two zones are divided by vaporization temperatures, above which water will be vaporized during the giant bubble nucleation. Water in the vaporization zone vaporizes when the bubble nucleation temperature is reached. This bubble nucleation temperature only depends on the absolute amount of gas dissolved in the water, while the vaporization temperature increases with water boiling points. As a result, the light-vapor conversion efficiency decreases with increasing boiling points.

This study of the light-vapor conversion efficiency of laser-irradiated Au nanoparticles in water is also relevant for applications. For example, noble-metal nanoparticles are one of the most commonly used solar energy absorbers. Our study demonstrates that the interfacial (localized) heating can significantly increase the solar-vapor conversion efficiency [36–38].

ACKNOWLEDGMENTS

TABLE I. Physicochemical properties of water under ambient pressure of 1 and 10 bar [35]. All values are taken at 25°C.

Parameters	1 bar	10 bar
Density ρ (kg/m^3)	997.05	1000.3
Thermal conductivity λ[mW/(m K)]	606.52	610.0
Thermal diffusivity κ ($\times 10^{-6}$ m^2/s)	0.146	0.145
Latent heat of vaporization H_{vap} (kJ/kg)	104.92	113.48
Specific-heat capacity c_p [kJ/(kg K)]	4.1813	4.1973

APPENDIX: PHYSICOCHEMICAL PROPERTIES OF WATER UNDER DIFFERENT AMBIENT PRESSURES

The physicochemical properties of pure water under ambient pressures of 1 bar and 10 bar are listed in Table I. The results show that density ρ, thermal conductivity λ, thermal diffusivity κ, latent heat of vaporization H_{vap}, and specific-heat capacity c_p of pure water at 10 bar are very close to that at 1 bar. Therefore, we can assume that the above 4 parameters of water basically remain constant when ambient pressure changes from 1 to 9 bar.

[1] G. Baffou and R. Quidant, Nanoplasmonics for chemistry, Chem. Soc. Rev. **43**, 3898 (2014).

[2] M. T. Carlson, A. J. Green, and H. H. Richardson, Superheating water by cw excitation of gold nanodots, Nano Lett. **12**, 1534 (2012).

[3] Z. Fang, Y. Zhen, O. Neumann, A. Polman, F. Javier Garcia de Abajo, P. Nordlander, and N. J. Halas, Evolution of light-induced vapor generation at a liquid-immersed metallic nanoparticle, Nano Lett. **13**, 1736 (2013).

[4] S. Baral, A. J. Green, M. Y. Livshits, A. O. Govorov, and H. H. Richardson, Comparison of vapor formation of water at the solid/water interface to colloidal solutions using optically excited gold nanostructures, ACS Nano **8**, 1439 (2014).

[5] X. Liu, L. Bao, M. Dipalo, F. De Angelis, and X. Zhang, Formation and dissolution of microbubbles on highly-ordered plasmonic nanopillar arrays, Sci. Rep. **5**, 18515 (2015).

[6] Y. Wang, M. E. Zaytsev, G. Lajoinie, H. L. The, J. C. T. Eijkel, A. van den Berg, M. Versluis, B. M. Weckhuysen, X. Zhang, H. J. W. Zandvliet, and D. Lohse, Giant and explosive plasmonic bubbles by delayed nucleation, Proc. Natl. Acad. Sci. USA **115**, 7676 (2018).

[7] J. Shao, M. Xuan, L. Dai, T. Si, J. Li, and Q. He, Near-infrared-activated nanocalorifiers in microcapsules: Vapor bubble generation for in vivo enhanced cancer therapy, Angew. Chem. Int. Ed. **54**, 12782 (2015).

[8] E. Y. Lukianova-Hleb, E. Sassaroli, A. Jones, and D. O. Lapotko, Transient photothermal spectra of plasmonic nanobubbles, Langmuir **28**, 4858 (2012).

[9] D. Lapotko, Plasmonic nanoparticle-generated photothermal bubbles and their biomedical applications, Nanomedicine **4**, 813 (2009).

[10] Q. Fan, W. Hu, and A. T. Ohta, Laser-induced microbubble poration of localized single cells, Lab Chip **14**, 1572 (2014).

[11] J. R. Adleman, D. A. Boyd, D. G. Goodwin, and D. Psaltis, Heterogenous catalysis mediated by plasmon heating, Nano Lett. **9**, 4417 (2009).

[12] L. Lin, X. Peng, Z. Mao, W. Li, M. N. Yogeesh, B. B. Rajeeva, E. P. Perillo, A. K. Dunn, D. Akinwande, and Y. Zheng, Bubble-pen lithography, Nano Lett. **16**, 701 (2016).

[13] Y. Xie and C. Zhao, An optothermally generated surface bubble and its applications, Nanoscale **9**, 6622 (2017).

[14] F. Tantussi, G. C. Messina, R. Capozza, M. Dipalo, L. Lovato, and A. F. De, Long-range capture and delivery of water-dispersed nano-objects by microbubbles generated on 3d plasmonic surfaces, ACS Nano **12**, 4116 (2018).

[15] O. Neumann, C. Feronti, A. D. Neumann, A. J. Dong, K. Schell, B. Lu, E. Kim, M. Quinn, S. Thompson, N. Grady *et al.*, Compact solar autoclave based on steam generation using broadband light-harvesting nanoparticles, Proc. Natl. Acad. Sci. USA **110**, 11677 (2013).

[16] S. V. Boriskina, H. Ghasemi, and G. Chen, Plasmonic materials for energy: From physics to applications, Mater. Today **16**, 375 (2013).

[17] H. Ghasemi, G. Ni, A. M. Marconnet, J. Loomis, S. Yerci, N. Miljkovic, and G. Chen, Solar steam generation by heat localization, Nat. Commun. **5**, 4449 (2014).

[18] X. Wang, Y. He, X. Liu, G. Cheng, and J. Zhu, Solar steam generation through bio-inspired interface heating of broadband-absorbing plasmonic membranes, Appl. Energy **195**, 414 (2017).

[19] H. Jin, G. Lin, L. Bai, A. Zeiny, and D. Wen, Steam generation in a nanoparticle-based solar receiver, Nano Energy **28**, 397 (2016).

[20] L. Zhou, S. D. Zhuang, C. Y. He, Y. L. Tan, Z. L. Wang, and J. Zhu, Self-assembled spectrum selective plasmonic absorbers with tunable bandwidth for solar energy conversion, Nano Energy **32**, 195 (2017).

[21] L. Zhou, Y. Tan, J. Wang, W. Xu, Y. Yuan, W. Cai, S. Zhu, and J. Zhu, 3D self-assembly of aluminium nanoparticles for plasmon-enhanced solar desalination, Nat. Photon. **10**, 393 (2016).

[22] M. E. Zaytsev, G. Lajoinie, Y. Wang, D. Lohse, H. J. W. Zandvliet, and X. Zhang, Plasmonic bubbles in n-Alkanes, J. Phys. Chem. C **122**, 28375 (2018).

[23] Y. Wang, M. E. Zaytsev, H. L. The, J. C. T. Eijkel, H. J. W. Zandvliet, X. Zhang, and D. Lohse, Vapor and gas-bubble growth dynamics around laser-irradiated, water-immersed plasmonic nanoparticles, ACS Nano **11**, 2045 (2017).

[24] X. Li, Y. Wang, B. Zeng, M. Detert, A. Prosperetti, H. J. Zandvliet, and D. Lohse, Plasmonic microbubble dynamics in binary liquids, J. Phys. Chem. Lett. **11**, 8631 (2020).

[25] H. Le-The, E. Berenschot, R. M. Tiggelaar, N. R. Tas, A. van den Berg, and J. C. T. Eijkel, Shrinkage control of photoresist for large-area fabrication of sub-30 nm periodic nanocolumns, Adv. Mater. Technol. **2**, 1600238 (2017).

[26] Y. Wang, T. Lu, X. Li, and H. Wang, Automated image segmentation-assisted flattening of atomic force microscopy images, Beilstein J. Nanotechnol. **9**, 975 (2018).

[27] Y. Wang, T. Lu, X. Li, S. Ren, and S. Bi, Robust nanobubble and nanodroplet segmentation in atomic force microscope images using the spherical Hough transform, Beilstein J. Nanotechnol. **8**, 2572 (2017).

[28] Y. Wang, Z. Zhang, H. Wang, and S. Bi, Segmentation of the clustered cells with optimized boundary detection in negative phase contrast images, PLoS ONE **10**, e0130178 (2015).

[29] V. Skripov and P. Pavlov, Explosive boiling of liquids and fluctuation nucleus formation, Teplofiz. Vys. Temp. **8**, 782 (1970).

[30] M. Blander and J. L. Katz, Bubble nucleation in liquids, Adv. Colloid Interface Sci. **10**, 1 (1975).

[31] S. Puchinskis and P. Skripov, The attainable superheat: From simple to polymeric liquids, Int. J. Thermophys. **22**, 1755 (2001).

[32] J. Lombard, T. Biben, and S. Merabia, Kinetics of Nanobubble Generation Around Overheated Nanoparticles, Phys. Rev. Lett. **112**, 105701 (2014).

[33] G. V. Hartland, L. V. Besteiro, P. Johns, and A. O. Govorov, What's so hot about electrons in metal nanoparticles? ACS Energy Lett. **2**, 1641 (2017).

[34] X. Li, Y. Wang, M. E. Zaytsev, G. Lajoinie, H. Le-The, J. G. Bomer, J. C. T. Eijkel, H. J. W. Zandvliet, X. Zhang, and D. Lohse, Plasmonic bubble nucleation and growth in water: the effect of dissolved air, J. Phys. Chem. C **123**, 23586 (2019).

[35] W. M. Haynes, *CRC Handbook of Chemistry and Physics* (CRC Press, Boca Raton, FL, 2014).

[36] N. Xu, X. Hu, W. Xu, X. Li, L. Zhou, S. Zhu, and J. Zhu, Mushrooms as efficient solar steam-generation devices, Adv. Mater. **29**, 1606762 (2017).

[37] L. Zhou, X. Li, G. W. Ni, S. Zhu, and J. Zhu, The revival of thermal utilization from the sun: interfacial solar vapor generation, Natl. Sci. Rev. **6**, 562 (2019).

[38] X. Wang, X. Li, G. Liu, J. Li, X. Hu, N. Xu, W. Zhao, B. Zhu, and J. Zhu, An interfacial solar heating assisted liquid sorbent atmospheric water generator, Angew. Chem. Int. Ed. **58**, 12054 (2019).